

Available online at www.sciencedirect.com

ScienceDirect

journal homepage: www.elsevier.com/locate/AJPS

Original Research Paper

Low-temperature photothermal-induced alkyl radical release facilitates dihydroartemisinin-triggered “valve-off” starvation therapy



Xiaomin Su^{a,b,1}, Boshu Ouyang^{c,1}, Yao Liu^d, Yang Wang^a, Ruizhe Xu^e, Lili Niu^a, NanNan Li^a, Ce Xu^a, Zanya Sun^a, Huishu Guo^{a,*}, Zhiqing Pang^{e,*}, Xiangrong Yu^{b,*}

^a Central Laboratory, First Affiliated Hospital, Institute (College) of Integrative Medicine, Dalian Medical University, Dalian 116021, China

^b Department of Radiology, Zhuhai People's Hospital, Zhuhai Hospital affiliated with Jinan University, Zhuhai 519000, China

^c Department of Integrative Medicine, Huashan Hospital, Fudan University, Shanghai 200040, China

^d The Institute for Translational Nanomedicine, Shanghai East Hospital, Tongji University School of Medicine, Shanghai 200120, China

^e School of Pharmacy & Key Laboratory of Smart Drug Delivery, Fudan University, Shanghai 201203, China

ARTICLE INFO

Article history:

Received 20 May 2023

Revised 23 August 2023

Accepted 25 August 2023

Available online 30 September 2023

Keywords:

Starvation therapy

Alkyl radicals

Hydrogel

Ink

Low-temperature photothermal

ABSTRACT

The high nutrient and energy demand of tumor cells compared to normal cells to sustain rapid proliferation offer a potentially auspicious avenue for implementing starvation therapy. However, conventional starvation therapy, such as glucose exhaustion and vascular thrombosis, can lead to systemic toxicity and exacerbate tumor hypoxia. Herein, we developed a new “valve-off” starvation tactic, which was accomplished by closing the valve of glucose transporter protein 1 (GLUT1). Specifically, dihydroartemisinin (DHA), 2,20-azobis [2-(2-imidazolin-2-yl) propane] dihydrochloride (AI), and Ink were co-encapsulated in a sodium alginate (ALG) hydrogel. Upon irradiation with the 1064 nm laser, AI rapidly disintegrated into alkyl radicals (R[•]), which exacerbated the DHA-induced mitochondrial damage through the generation of reactive oxygen species and further reduced the synthesis of adenosine triphosphate (ATP). Simultaneously, the production of R[•] facilitated DHA-induced starvation therapy by suppressing GLUT1, which in turn reduced glucose uptake. Systematic *in vivo* and *in vitro* results suggested that this radical-enhanced “valve-off” strategy for inducing tumor cell starvation was effective in reducing glucose uptake and ATP levels. This integrated strategy induces tumor starvation with efficient tumor suppression, creating a new avenue for controlled, precise, and concerted tumor therapy.

© 2023 Published by Elsevier B.V. on behalf of Shenyang Pharmaceutical University.

This is an open access article under the CC BY-NC-ND license

(<http://creativecommons.org/licenses/by-nc-nd/4.0/>)

* Corresponding authors.

E-mail addresses: guohuishu1@126.com (H. Guo), zqpang@fudan.edu.cn (Z. Pang), yxr00125040@126.com (X. Yu).

¹ These authors contributed equally to this work.

Peer review under responsibility of Shenyang Pharmaceutical University.

1. Introduction

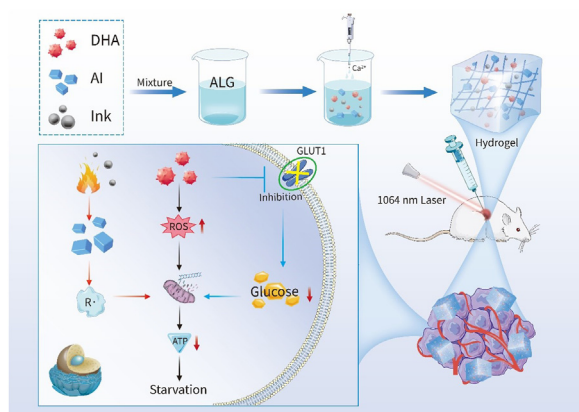
Aberrant cellular metabolism and excessive nutrient depletion are major physiological features of tumors. Therefore, starvation therapy for tumors by obstructing blood supply and consuming critical nutrients has been extensively explored as an attractive approach for tumor therapy [1]. Warburg discovered that tumor cells have an increased demand for glucose uptake, which promotes tumor growth and proliferation by means of anaerobic glycolysis [2]. Due to the metabolic characteristics of tumor cells, two starvation therapies have been developed as potential treatments for neoplasms: glucose starvation and vascular embolization [1,3,4]. Glucose oxidase (GOx) has gained attention as a potential starvation-inducing drug that can effectually exhaust glucose in tumor cells. However, GOx has some unavoidable limitations in the treatment of tumors. One possible perspective is that the excess H_2O_2 produced by glucose oxidation not only accelerates tumor metastasis and invasion, but also inevitably causes oxidative damage to neighboring normal tissues [5]. On the other hand, the higher toxicity and instability of GOx limit its anti-tumor effect [6]. Vascular embolization has been considered as a potential strategy for inducing starvation therapy by blocking blood flow to tumors. Nevertheless, the efficacy of this approach can be influenced by rapid blood flow, resulting in the formation of ineffective embolization or plaque. Therefore, innovative and effective strategies need to be urgently developed to overcome these challenges.

Glucose transport proteins (GLUTs) are a class of transmembrane proteins that perform a key function in the regulation of glucose transport across the cell membranes [7]. As important “valves” regulating glucose uptake, GLUTs are expressed at high levels in many tumor cells to support rapid tumor proliferation [8]. Notably, among the human GLUT family, GLUT1 has been shown to be significantly upregulated in various types of tumors and is considered a primary prognostic marker for tumorigenesis [9]. Although nanomedicines targeting GLUT1 to mediate endocytosis have been explored, few studies have investigated the efficacy of starvation strategies achieved through inhibiting GLUT1. Therefore, we developed a novel starvation strategy for GLUT1 inhibition by DHA. DHA is a first-generation offshoot of artemisinin that was initially developed to treat malaria with globally recognized effective treatment and low toxicity [10]. Interestingly, the biological activity of DHA extends beyond its anti-malarial properties. Similar to many naturally occurring compounds, DHA has demonstrated anti-tumor effects through a range of mechanisms, such as suppression of angiogenesis and proliferation, induction of ferroptosis, and increased cellular oxidative stress [11,12]. For instance, Wang et al. designed and synthesized DHA nanoparticles that respond to both intracellular acidity and oxidative stress, allowing for the co-delivery of DHA and glutathione peroxidase 4 inhibitor RSL-3. This delivery system ultimately induced ferroptosis in pancreatic ductal cancer cells [13]. Moreover, Liu et al. developed a new nanomedicine called Tf@IR820-DHA, which promoted cancer immunity by inducing cellular triple oxidative stress [14]. Although DHA

has received considerable attention as a promising antitumor agent, studies on DHA-induced cell starvation through GLUT1 inhibition have been sparsely reported. Therefore, we will conduct further investigation on DHA-induced cell starvation.

Tumor elimination by cytotoxic free radicals has been considered as a promising strategy. However, an oxygen-deprived neoplasm microenvironment may compromise the generation of ROS, making the therapeutic effect much less effective [15]. AI possesses excellent water solubility and can undergo thermal decomposition to produce R^{\cdot} , which remains unaffected by the hypoxic microenvironment of tumors [16]. AI has shown favorable antitumor effects and has garnered widespread interest. For example, Chen et al. designed a new $Nb_2C@mSiO_2$ nanosheet to achieve effective antitumor effect by photothermal decomposition of AI [17]. Furthermore, our previous work has demonstrated that AI conjoined with low-temperature photothermal treatment accomplished antitumor effect through lipid oxidation [18]. Although the association of low-temperature photothermal with R^{\cdot} for tumor treatment has been extensively reported, the question of whether ROS can promote DHA-induced starvation by damaging mitochondria has not yet been explored.

The present study proposes a novel approach that utilizes R^{\cdot} enhanced DHA-induced cell starvation therapy to improve the effectiveness of antitumor treatment. Specifically, the versatile ALG was applied to react with Ca^{2+} to form on-site hydrogels for encapsulating DHA, AI, and Ink and inducing tumor cell starvation by simple intratumoral injection. ALG is a naturally occurring polysaccharide comprised of α -L-guluronic acid and β -D-mannuronic acid, which can rapidly chelate with Ca^{2+} to produce a gelatinous “egg box” construct [19]. ALG possesses several advantageous properties that make it a suitable material for various biomedical applications, including drug delivery. Besides the capability to generate hydrogels *in situ*, ALG presents favorable biocompatibility and biodegradability properties, which are crucial factors to consider for its implementation *in vivo* [20]. Compared to other types of gels, ALG has been extensively employed in drug delivery, cell transplantation, and wound healing, owing to the outstanding features including suppleness, non-toxicity, high-water content and extracellular matrix-like construction [21–23]. Chinese traditional Ink was applied as a photothermal agent due to the good photothermal properties and excellent biocompatibility [24]. As illustrated in Scheme 1, DHA, AI, Ink, and ALG were briefly mixed and administered into the tumor by a minimally invasive method. Upon exposure to a 1064 nm laser, the resultant elevated temperature led to the catabolism of AI into alkyl radicals, which subsequently caused mitochondrial damage. DHA not only inhibited the expression of GLUT1 to reduce the cellular uptake of glucose, but also induced ROS production by reacting with intracellular Fe^{2+} . Thus, R^{\cdot} and DHA-generated ROS worked synergistically to further damage mitochondria, which in turn enhanced DHA-induced cellular starvation therapy by reducing ATP synthesis. This “off-valve” starvation strategy provides guidance for tumor treatment and may become a breakthrough in tumor therapy. This starvation therapy, induced by the dual effect of cutting off energy supply from the outside and damaging mitochondria from the inside, demonstrated potent anti-tumor effects.



Scheme 1 – Schematic diagram of DHA/AI/Ink@ALG-induced cell starvation therapy.

2. Materials and methods

2.1. Materials

Hu-Ink was supplied by Hu Kai wen Ink Factory. AI and 2,2-Azobis (3-ethylbenzothiazoline-6-sulfonic acid) (ABTS) were obtained from Macklin. DHA and Cell counting kit-8 (CCK-8) was supplied by Solarbio Science & Technology Co. Ltd. ALG and Calcium chloride were provided by Aladdin. ATP and BCA protein assay kit were purchased from Beyotime. Live and Dead Dye Kit, Annexin-V-FITC/PI, and Hoechst 33,258 were the products of KeyGen Biotech. 2-Deoxy-2-[(7-nitro-2,1,3-benzoxadiazol-4-yl) amino]-D-glucose (2-NBDG) was provided by Amgicam. GLUT1 antibodies and TUNEL kits were offered by absin. Roswell Park Memorial Institute 1640 cell culture medium and 0.25% trypsin solution were provided by MeilunBio.

2.2. Synthesis and characterization of hydrogel

To verify the gel-forming properties of ALG, different concentrations of ALG were blended well with the fixed concentration of Ink (1 mg/ml). Then, the mixed solution was poured into a beaker that contained 7 ml CaCl₂ solution. Photographs were taken at various times to observe the gel-forming properties of ALG. Subsequently, the mixed solution of Ink and Ink@ALG (Ink 1 mg/ml; ALG 5 mg/ml) were also recorded at different times by the same method.

Firstly, the Zetasizer Nano ZS was used to measure the particle diameter and zeta potential of the Ink. ALG was mixed with AI, DHA, and Ink with homogenization by sonication. Finally, electron micrographs of the hydrogels were taken with a Zeiss Gemini 300 scanning electron microscope (SEM).

To verify the success of drug encapsulation, Ink, AI, DHA, ALG, and DHA/AI/Ink@ALG were scanned with ultraviolet spectrophotometry (UV-vis) at wavelengths of 300–1,000 nm, respectively. In order to prove that ALG hydrogel could be used for drug transport, the drug release of DHA/AI/Ink@ALG hydrogel was measured by spectrophotometry. Specifically, AI@ALG, Ink@ALG, and DHA@ALG were injected into a Ca²⁺

containing solution and transferred to a dialysis bag into PBS with media of pH 7.4 and 6.5. It was placed into a constant temperature shaking bed for shaking, 1 ml liquid was taken at different time points, and then another 1 ml liquid was filled into it. Finally, the drug release was measured at different time points. At the same time, photos of DHA/AI/Ink@ALG at 0 h and 48 h were taken to prove the release of the drug.

2.3. Detection of photothermal properties

To investigate the photothermal characteristics of Ink, various concentrations of Ink were subjected to irradiation with a 1064 nm laser (0.5 W/cm² 10 min). The temperature variations at various times during the laser exposure were monitored, and thermal images were captured using a near-infrared (NIR) thermal camera. Moreover, the photothermal characteristics of hydrogels were evaluated using the same protocol for various groups, including H₂O, ALG, Ink, DHA, Ink@ALG, AI/Ink@ALG, and DHA/AI/Ink@ALG.

To explore the photothermal stability, various groups including Ink and DHA/AI/Ink@ALG were subjected to irradiation with a 1064 nm laser for 5 min, followed by cooling at room temperature for 5 min. This was performed five times and the temperature changes at different time points were recorded.

2.4. Detection of free radicals

ABTS was used as a probe for free radical detection. Specifically, ABTS (2 mg/ml) and AI (200 µg/ml) were mixed well and reacted in the water bath at 37 °C and 44 °C for different times. UV-vis was used to measure the absorbance of each solution at 400–900 nm. To further explore the generation of R[•] under laser irradiation, the solutions subjected to the 1064 nm laser were further measured. Specifically, a mixture of 0.2 ml of DHA/AI/Ink and 0.2 ml ABTS (2 mg/ml) was exposed to a 1064 nm laser (0.5 W/cm²) for different times. The absorbance of each solution was subsequently determined using UV-vis spectrophotometry over a range of 400–900 nm.

To detect the formation of R[•] in cells, the fluorescent probe DCFH-DA was employed. Briefly, HepG2 cells were cultured on the 20 mm confocal dish and incubated for overnight before being exposed to various experimental conditions. Subsequently, the cells were subjected to irradiation with a 1064 nm laser (0.5 W/cm²) for 10 min. Following irradiation, the cells were washed and incubated with DCFH-DA in the absence of light for 30 min. Finally, the fluorescence of DCF was visualized using either CLSM or flow cytometry.

2.5. In vitro synergistic antitumor effect

HepG2 cells were inoculated in 96-well plates with a concentration of 1.5×10^4 per well and cultured overnight. Subsequently, the cells were treated with various formulations, including DHA, Ink, AI, ALG, AI/Ink, DHA/AI/Ink, and DHA/AI/Ink@ALG for 12 h. After this, the cells were incubated for an additional 12 h with or without irradiation by a 1064 nm laser. The culture solution was then replaced with a solution of CCK-8 reagent, which was diluted in the cell culture medium at a ratio of 10:1. The cells were subsequently

incubated at a temperature of 37 °C for a duration of 1 h, after which the absorption at a wavelength of 450 nm was quantified using a microplate reader.

Live-dead cell staining was used to visualize cell death after HepG2 treatment in different groups. Specifically, the cells were spread on 20 mm confocal discs and incubated overnight. The experimental groups, including DHA, AI, Ink, AI/Ink, DHA/AI/Ink, and GA/AI/Ink@ALG (DHA 35 µM, AI 100 µg/ml, Ink 25 µg/ml, and 500 µg/ml), were joined to confocal dishes and hatched for 6 h. Thereafter, the cells were exposed to a 1064 nm laser (0.5 W/cm²) for a duration of 10 min, or were left unexposed, and cultured for a further 6 h. Finally, the cells were cleaned and incubated with Calcein-AM/PI at a temperature of 37 °C, shielded from light, for a period of 30 min. The excess dye was subsequently washed away with PBS and photographed for observation with CLSM.

Annexin V apoptosis detection kits were further employed to detect apoptosis. Cells were collected after different treatments and stained with Annexin V and propidium iodide. Finally, the cells were detected by flow cytometry after 15 min of staining and analyzed by FlowJo.

2.6. Measurement of mitochondrial membrane potential

JC-1 was employed as a probe to determine the change in mitochondrial membrane potential ($\Delta\Psi_m$). Briefly, HepG2 were inoculated in 12-well plates and cultured overnight. Cells were treated in different experimental groups and stained with 200 µl working solution at 37 °C for 25 min. Afterwards, the cells were examined by flow cytometry.

2.7. Assay of intracellular ATP

The levels of intracellular ATP in HepG2 cells after different treatments were assayed with an ATP kit. Briefly, 12-well plates were inoculated with cells and cultured overnight. The cells were then treated with different formulations. After treatment, the cells were lysed and the ATP levels were assayed following the instructions. The amount of ATP was quantified by measuring the amount of luminescence with a microtiter plate.

2.8. Western blot

Briefly, the 6-well plates were inoculated with HepG2 cells and cultured overnight. Then, the cells were collected and lysed after different groups of treatment. The cells were processed according to standard instructions. An inner parameter of β -actin was employed for comparison.

2.9. Intracellular glucose uptake experiments

The intracellular glucose uptake was detected with 2-NBDG. Briefly, the 12-well plates were inoculated with HepG2 cells and cultured overnight. Cells were treated with a sugar-free medium for 12 h. Then, the solution was withdrawn and 2-NBDG was joined for incubation for 30 min at 37 °C without light. Finally, cells were collected after washing twice with PBS. The cells were detected by flow cytometry and FlowJo was performed for analysis.

2.10. In vivo immobilization of hydrogels

To further examine the drug immobilization capability of ALG, intra-tumoral injections of ICG solution alone and ICG@ALG hydrogel (ICG 200 µg/ml, ALG 5 mg/ml) were carried out, and photographs were captured using fluorescence *in vivo* imaging at various time intervals. Additionally, Ink and Ink@ALG hydrogels were subcutaneously injected, and the skin tissue was incised after 48 h for observation.

2.11. In vivo antitumor efficacy

The *in vivo* antitumor effect was studied in nude mice bearing HepG2 tumors. Specifically, once the subcutaneous tumors reached around 100 mm³, mice were randomly assigned to 5 groups ($n = 5$) and treated with different formulations. Subcutaneous drug injections and 1064 nm laser irradiation were performed on Days 0 and 3. After the first therapy, the tumors size and mouse weight were noted for 15 d consecutively. The tumor volume (V) and tumor suppression ratio (SR) were computed based on the following formulation. At Day 15, the tumors and major organs were removed for H&E and TUNEL staining to evaluate the anti-tumor effect and biological safety.

$$V(\text{mm}^3) = (\text{length} \times \text{width}^2) / 2$$

$$\text{SR}(\%) = (W_{\text{blank}} - W_{\text{treat}}) / W_{\text{blank}} \times 100\%$$

2.12. Statistical analysis

All data are indicated as mean \pm SD (standard deviation). Statistical analysis was carried out by two-way ANOVA. * $P < 0.05$, ** $P < 0.01$, and *** $P < 0.001$ were significantly different.

3. Results and discussions

3.1. Synthesis and characterization of hydrogel

ALG is a polysaccharide with good solubility in water and reacts with Ca²⁺ to become an “egg box” crosslinked hydrogel [20,25]. To investigate the hydrogel formation properties of ALG in Ca²⁺ solution at different concentrations, 1.8 mM Ca²⁺ solution was selected to simulate the physiological concentration [26]. Based on the colorless and transparent nature of ALG, Ink was employed to assess its gel-forming properties. As illustrated in Fig. S1, when the solution containing Ca²⁺ was injected into the ALG at the concentration of 1 mg/ml, the solution swiftly spread into the beaker as a result of the weaker gel-forming properties. However, when the ALG concentration surpassed 5 mg/ml, the Ink@ALG solution quickly gelled as it was pushed out of the tip of the needle, and no morphological changes were visible within 1 h. It should be noted that at concentrations above 10 mg/ml, the viscosity of ALG was so high that injection became impractical. Finally, 5 mg/ml of ALG was selected for subsequent experimental studies. In contrast, upon injection into the Ca²⁺-containing solution, the free Ink solution

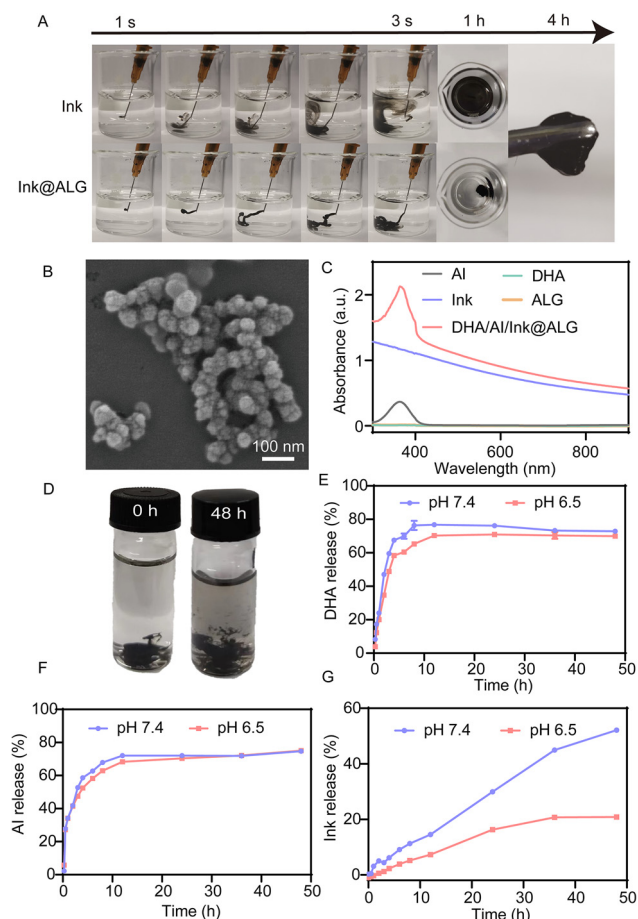


Fig. 1 – Characteristics of hydrogel DHA/AI/Ink@ALG. (A) Pictures of Ink and Ink@ALG injected into Ca^{2+} -containing solution at different time points. (B) SEM images of DHA/AI/Ink@ALG. (C) UV-vis of different formulations. (D) Photographs of drug release from DHA/AI/Ink@ALG hydrogels at 0 h and 48 h. Release curves of DHA (E), AI (F) and Ink (G) from ALG hydrogel at different time points.

quickly dispersed throughout the beaker, as illustrated in Fig. 1A. This observation provides evidence that ALG can react with Ca^{2+} *in vitro*, leading to the formation of hydrogels. To further investigate the properties of the gels, rheometers were employed to examine the rheology and viscosity of hydrogels. In rheological analysis experiments, when the elastic modulus (G') is greater than the viscosity modulus (G''), the sample is defined as a solid rather than a liquid [26,27]. As shown in Fig. S2A, G' was significantly larger than G'' , indicating that ALG could form hydrogels by chelation with Ca^{2+} . In addition, we also explored the relationship between the viscosity of the hydrogel and the shear rate, as shown in Fig. S2B, the viscosity of the DHA/AI/Ink@ALG hydrogel gradually decreased with the increase of the shear rate, signifying the presence of shear thinning behavior within the hydrogel. While the viscosity of the DHA/AI/Ink@ALG solution did not exhibit significant changes.

The dynamic light scattering (DLS) detector was employed to evaluate the particle size and zeta potential of Ink. The results showed that the z-average diameter and potential of Ink were approximately 181.78 nm and -19.80 mV,

respectively (Fig. S3). Subsequently, the morphology of the DHA/AI/Ink@ALG was described by SEM. Based on the visualization presented in Fig. 1B, a significant population of Ink nanoparticles were aggregated on the hydrogels surface. This outcome implied that the crosslinking of ALG with Ca^{2+} had demonstrated an effective ability to immobilize Ink within the hydrogels. To further demonstrate that the drug was encapsulated in the ALG solution, UV-vis was performed to determine the wavelengths of AI, Ink, ALG, DHA and DHA/AI/Ink@ALG within the scope of 300–900 nm. As shown in Fig. 1C, the absorption spectrum of AI exhibited a distinctive peak at 360 nm. Meanwhile, Ink demonstrated a high level of absorbance, indicating its potential as a photothermal agent for near infrared II (NIR-II). Whereas DHA/AI/Ink@ALG had the characteristic absorption peaks of AI, DHA, and Ink, indicating that AI, DHA, and Ink were encapsulated in ALG.

Constant temperature shaker experiments were employed to simulate the kinetics of the drug *in vivo*. As shown in Fig. 1D, the DHA/AI/Ink@ALG solution changed from colorless to ebony after 48 h of constant temperature oscillation, confirming that a portion of the drug was released from the ALG and Ca^{2+} crosslink. To further explore the drug release profile graph, the drug release was measured at different time points. As shown in Fig. 1E-G, there was a burst of DHA and AI release before 8 h, with release reaching about 60%, but the drug release leveled off after 8 h. It is also noteworthy that drug release in the first 12 h exhibited a slightly higher level in the pH 7.4 environment compared to the tumor micro-acidic environment at pH 6.5. This may be attributed to the deprotonation of carboxylic acid groups on the ALG leading to an increase in osmosis as pH increases, which in turn leads to network swelling and drug release [20,25,28,29]. Furthermore, we observed a slower release rate for Ink compared to DHA and AI, as depicted in Fig. 1G. This distinction can be attributed to the larger particle size of Ink, which operates as a nanoparticle rather than a free drug. Overall, these findings suggested that the gel possesses a non-compact structure, establishing its potential as a viable drug delivery vehicle.

3.2. Detection of photothermal properties and free radicals

Previous research has demonstrated that Ink exhibits powerful absorbance within the NIR-II range [30]. Firstly, we investigated the photothermal properties of Ink at different concentrations, with a consistent irradiation time. As illustrated in Fig. 2A, the temperature was progressively raised as the concentration of the Ink increased, indicating a concentration-dependent elevation of the temperature. When the Ink concentration was 25 $\mu\text{g}/\text{ml}$, the temperature raised from 28.90 $^{\circ}\text{C}$ to approximately 44.90 $^{\circ}\text{C}$ within the first 5 min of irradiation, and remained relatively stable at around 44 $^{\circ}\text{C}$ for the following 5 min. To accomplish the result of low-temperature photothermal therapy (PTT), the concentration of 25 $\mu\text{g}/\text{ml}$ was selected for further investigation. Near infrared thermal imaging devices were employed to detect the variation in temperature (Fig. 2B and D). The performance of photothermal between different groups was further explored. As illustrated in Fig. 2C, the temperature rise was

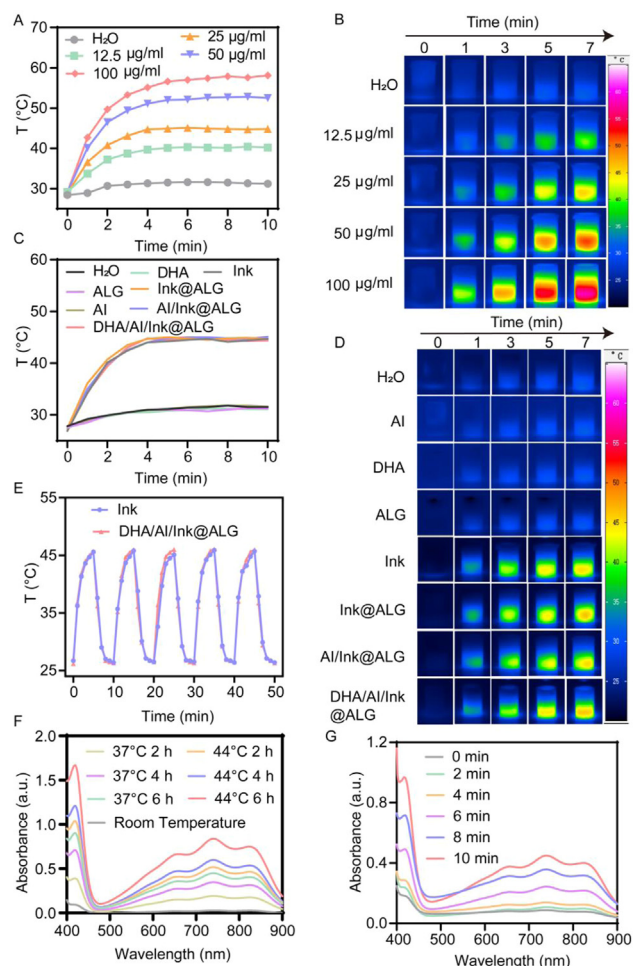


Fig. 2 – Photothermal properties of DHA/AI/Ink@ALG gels and release of free radicals. (A) Temperature profiles of Ink irradiated by 1064 nm laser for 10 min (0.5 W/cm^2) at different concentrations and (B) the associated photothermal images. (C) Curves of temperature changes in different groups under 1064 nm laser irradiation (0.5 W/cm^2) and (D) the corresponding diagrams of photothermal. (E) Photothermal stability of DHA/AI/Ink@ALG after 5 laser on-off cycles. (F) $\text{ABTS}^{+\bullet}$ production capacity when AI and ABTS are incubated in a water bath for different times and temperatures. (G) UV-vis absorption spectra of $\text{ABTS}^{+\bullet}$ at different times of 1064 nm laser irradiation.

negligible in the H_2O , AI, DHA, and ALG groups, whereas the Ink, Ink@ALG, AI/Ink@ALG, and DHA/AI/Ink@ALG groups showed noticeable and generally consistent temperature increase curves. The results indicated that the temperature increase was a consequence of the transformation of light energy into thermal energy via the photosensitizer Ink. In addition, we assessed the photothermal stability of Ink and DHA/AI/Ink@ALG. As presented in Fig. 2E, the temperature changes were recorded after 5 rounds of on-off illumination of a 1064 nm laser. The results showed that the Ink and DHA/AI/Ink@ALG groups exhibited no noticeable attenuation in photothermal performance throughout the process, indicating excellent photothermal stability of

DHA/AI/Ink@ALG. These findings suggested that Ink could be effectively used as a photothermal agent to induce AI decomposition.

To explore the decomposition ability of AI, ABTS was applied as a probe, which reacts with R' to form green $\text{ABTS}^{+\bullet}$ with a characteristic UV absorption wavelength between 400 and 900 nm. The ability of AI to decompose into R' was explored by examining the UV absorption spectra of $\text{ABTS}^{+\bullet}$. As depicted in Fig. 2F, the UV absorbance at 44 °C was significantly greater than that at 37 °C for the equal duration of incubation, indicating that the degradation of AI manifested a temperature-dependent behavior. Moreover, the relationship between the decomposition ability of AI and time was also investigated by incubating ABTS and AI at the same temperature. The findings demonstrated that the UV absorbance at 6 h was considerably greater than that at 2 h and 4 h, suggesting that AI generated more R' at higher temperature or extended incubation duration. Furthermore, the ability of $\text{ABTS}^{+\bullet}$ production at different times under 1064 nm laser illumination was also explored. As illustrated in Fig. 2F and S4, the absorbance of $\text{ABTS}^{+\bullet}$ gradually increased, and the color of the solution deepened progressively with the prolonged irradiation time, indicating an enhanced decomposition ability of AI.

3.3. Anti-tumor effect in vitro

To investigate the therapeutic potential of DHA/AI/Ink@ALG, the CCK-8 experiments were carried out to assess the effects on cell viability. Specifically, we implanted cells in 96-well plates and treated with medium containing different concentrations of Ink. The CCK-8 cytotoxicity experiments were conducted to measure the cell viability. First, we investigated the cytotoxicity of Ink on human umbilical vein endothelial cells (HUVEC). When the concentration of Ink reaches 200 $\mu\text{g/ml}$, there was no significant decrease in cell viability, indicating that Ink has excellent biocompatibility (Fig. S5). We next explored the photothermal effect of Ink in HepG2 tumor cells. The results showed that there was only a marginal decrease in cell viability after 10 min of 1064 nm laser irradiation in the group treated with Ink at a concentration of 25 $\mu\text{g/ml}$ (Fig. 3A). Conversely, there was no significant decrease in cell viability in the group that did not receive laser irradiation. These findings implied that the mild photothermal effect of Ink might contribute to the slight reduction in tumor cell survival. Furthermore, no significant cytotoxicity was observed after treatment with AI, both with and without 1064 nm laser irradiation, indicating that AI could not be decomposed into R' in deficiency of photothermal agent (Fig. S6). Subsequently, we investigated the synergistic therapeutic effect of Ink and AI. As presented in Fig. 3B, the cytotoxicity of AI/Ink gradually increased with increasing AI concentration under 1064 nm laser irradiation. On the contrary, no marked cytotoxicity was observed without 1064 nm laser irradiation, further demonstrating that Ink could induce the decomposition of AI into R' . Furthermore, the cytotoxicity experiments induced by DHA were also investigated. As depicted in Fig. 3C, consistent with previous studies, DHA exerted anti-tumor effects, with cell viability declining to approximately 75.63% at concentrations up to

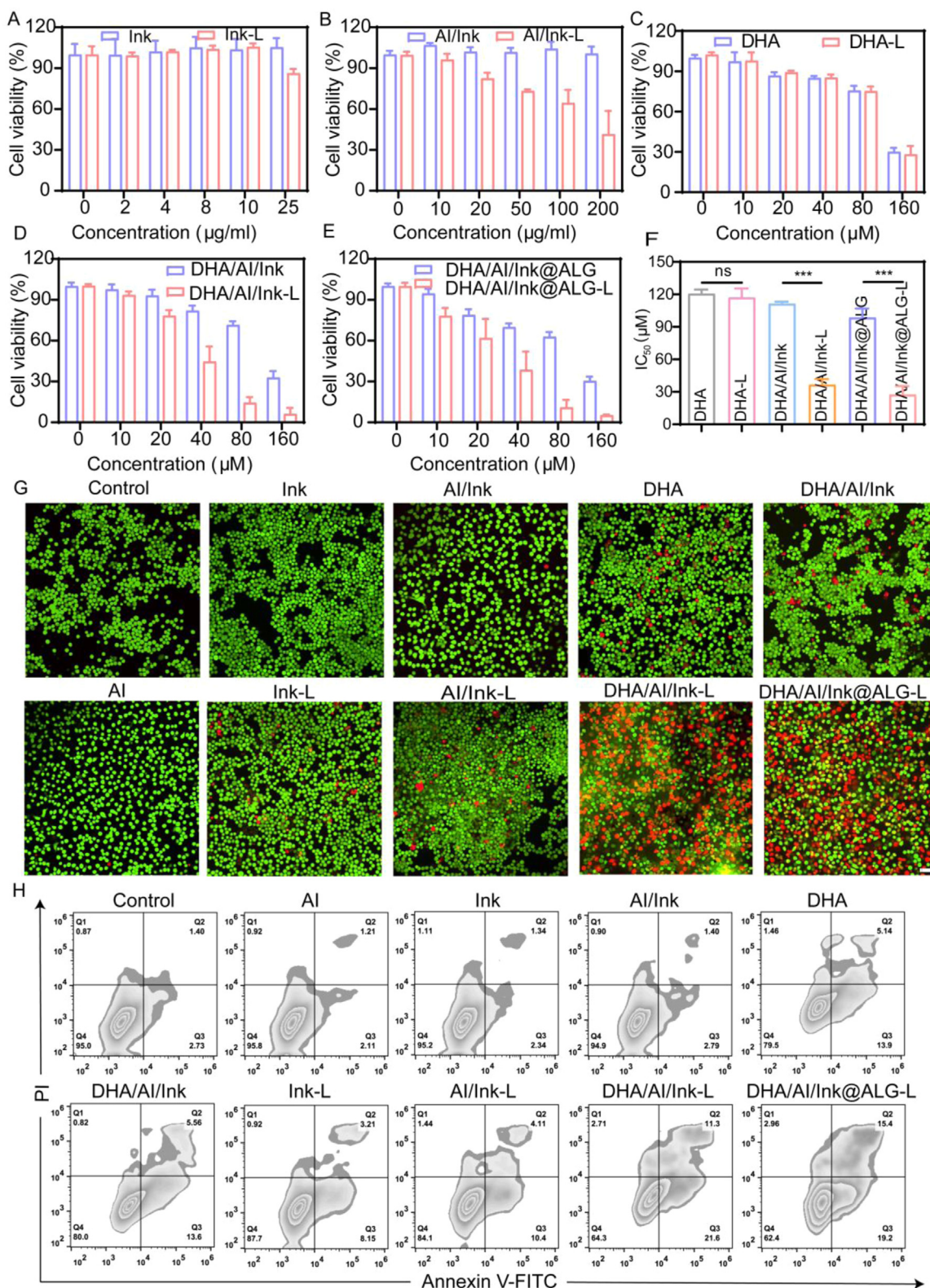


Fig. 3 – In vivo antitumor effect of DHA/AI/Ink@ALG. (A) Cell viability at different concentrations of Ink. **(B)** Cytotoxicity under constant concentration of Ink and increased concentration of AI. **(C)** Cell viability of HepG2 treated by elevated concentrations of DHA. **(D)** Cell viability of DHA/AI/Ink treated HepG2 cells by changing the concentration of DHA and the fixed concentrations of AI and Ink. **(E)** Cell viability of DHA/AI/Ink@ALG treated HepG2 cells by varying the concentration of DHA and the fixed concentrations of AI, Ink and ALG. (Each of the above groups was classified into a group with and without laser irradiation (0.5 W/cm², 10 mim). **(F)** Various groups of IC₅₀. **(G)** Confocal pictures of HepG2 cells incubated with different groups after co-staining with Calcein -AM (green) and PI (red) (Scale bars = 50 μm). **(H)** Apoptosis assay of HepG2 with different formulations after co-incubation with V-FITC/PI staining.

80 μM . The collaborative anti-tumor effect of AI and DHA was further explored. As illustrated in Fig. 3D, the cell viability exhibited a reduction that was dependent on the concentration of DHA. When the concentration of DHA reached 80 μM and was irradiated with a 1064 nm laser, the cell viability decreased to 14.37%, demonstrating that the R^{\cdot} decomposed by AI promoted the anti-tumor effect of DHA. Moreover, the half-inhibitory concentration (IC_{50}) of DHA/AI/Ink was 111.35 μM , apparently higher than that of the DHA/AI/Ink-L group (36.53 μM), further demonstrating that AI cannot be broken down into R^{\cdot} without laser irradiation. Finally, we further explored the cytotoxicity experiments of ALG. As demonstrated in Fig. 3E and S7, the cytotoxicity of ALG was not statistically significant, even at a concentration of 1 mg/ml. Besides, the synergistic antitumor effect of AI and DHA was not diminished by the addition of ALG, proving that ALG has good biocompatibility and could be used as a carrier for drug delivery. To further explore the biocompatibility of DHA/AI/Ink@ALG, 293T cells were treated with DHA/AI/Ink@ALG. The results showed that no significant decrease in cell viability when the concentration of DHA reached 40 μM , indicating that DHA/AI/Ink@ALG has favorable biocompatibility (Fig. S8).

Confocal fluorescence images of cells stained with (Calcein-AM)/PI following various sample treatments provided visual evidence that DHA and R^{\cdot} exhibited superior anti-cancer effects. As depicted in Fig. 3G, the AI, Ink, and AI/Ink groups exhibited no significant red fluorescence, suggesting that Ink has favorable biocompatibility and AI cannot be disassembled without 1064 nm laser irradiation. For cells cultured with Ink, AI/Ink and subjected to 1064 nm laser, a small fraction of PI-stained red cells was observed, implying that low-temperature photothermal had a mild antitumor effect. Similar gentle antitumor effects of DHA and DHA/AI/Ink can be seen from the large area of green fluorescence in the images. On the contrary, distinct large red fluorescent signals were observed in the DHA/AI/Ink-L and DHA/AI/Ink@ALG-L groups, denoting that a substantial number of dead cells were generated due to R^{\cdot} boost the DHA starvation therapy. Additionally, further quantitative flow cytometry results (Fig. 3H) revealed that the number of apoptotic cells in DHA/AI/Ink@ALG-treated cells exposed to 1064 nm laser were significantly greater than of DHA, demonstrating the synergistic tumoricidal effect of DHA and R^{\cdot} .

3.4. Investigation of anti-tumor mechanism

To elucidate the mechanism underlying the synergistic anti-tumor effect of DHA and R^{\cdot} , the fluorescent probe DCFH-DA was applied to monitor intracellular changes in ROS. The green fluorescence intensity was proportional to the ROS production level. As shown in Fig. 4A, there was no apparent green fluorescence emissions in the AI, Ink, and AI/Ink groups. However, relatively lower amounts of green fluorescence was detected in the AI/Ink group following exposure to 1064 nm laser illumination, indicating the production of a small amount of ROS through the photothermal decomposition of AI. Meaningfully, cells treated with DHA/AI/Ink@ALG or DHA/AI/Ink emitted a vivid green

fluorescence upon laser irradiation for 10 min. This striking phenomenon strongly suggested the substantial production of ROS resulting from the synergistic interplay between DHA and AI. In addition, the outcome demonstrated that ALG had a favourable biological compatibility and did not influence the generation of ROS. To further quantify the production of ROS, flow cytometry was utilized to analyze the results of different formulations of treatment of HepG2 cells. As revealed in Fig. 4B, the fluorescence strength of DHA/AI/Ink@ALG was approximately 3.8 times greater than control group, indicating that significant amounts of ROS were generated, which was agreement with the outcomes of confocal images. Remarkably, the flow cytometry results revealed slightly better fluorescence strength in the DHA group compared to the AI/Ink-L group, which could be ascribed to the production of ROS by DHA through the induction of endogenous ferritin autophagy [31]. It has been demonstrated that ROS are produced by mitochondria, but excessive ROS induce mitochondrial dysfunction and ultimately lead to a decrease in mitochondrial membrane potential ($\Delta\Psi\text{m}$) [32]. Accordingly, we further investigated the changes of $\Delta\Psi\text{m}$ after treating cells with various formulations. JC-1 was utilized as a probe to detect $\Delta\Psi\text{m}$, as it accumulates in the mitochondrial stroma and produces red luminescence when $\Delta\Psi\text{m}$ is high. In contrast, JC-1 emits green fluorescence in its monomeric form when $\Delta\Psi\text{m}$ is low. As shown in Fig. 4C, the ratios of red/green fluorescence were 2.51 and 1.95 after the administration of DHA and AI/Ink-L, respectively, indicating that only part of the $\Delta\Psi\text{m}$ was reduced by DHA and free radicals. However, when cells were treated with DHA/AI/Ink-L, a transition from red to green fluorescence was clearly observed, with a ratio of 0.36. This suggested that the breakdown of R^{\cdot} facilitated DHA-induced mitochondrial damage by generating of ROS.

Studies have shown that mitochondria are the main site of biological oxidation and energy conversion in cells, where most of the cellular ATP was produced by mitochondrial oxidative phosphorylation, which accounts for more than 80% of the energy required for life activities [33]. Thus, dysfunctional or impaired mitochondrial function can disrupt ATP synthesis, leading to decreased ATP production and cellular starvation. Fig. 4E illustrates that cells treated with AI, Ink, and AI/Ink did not exhibit a significant decline in ATP levels. However, DHA-treated cells demonstrated a mild decrease in intracellular ATP levels, suggesting that DHA induces mitochondrial damage through ROS and cellular starvation. In addition, the ATP levels in the DHA/AI/Ink-L group were significantly lower than those in the DHA group, which suggests that R^{\cdot} promote DHA-induced cellular starvation. It is well-established that tumor cells maintain abnormal metabolism because of cellular metabolic reprogramming [1]. As a characteristic feature of neoplastic cells, the Warburg effect signifies the high dependence of cancer cells on glycolysis for energy production over oxygen [2]. In order to examine the glycolysis of HepG2 cells following treatment with various formulations, a fluorescent probe called 2-NBDG was utilized to quantify glucose uptake by cells. As illustrated in Fig. 4D, the fluorescence intensity decreased remarkably after treatment with DHA/AI/Ink-L of cells compared to the control group, suggesting

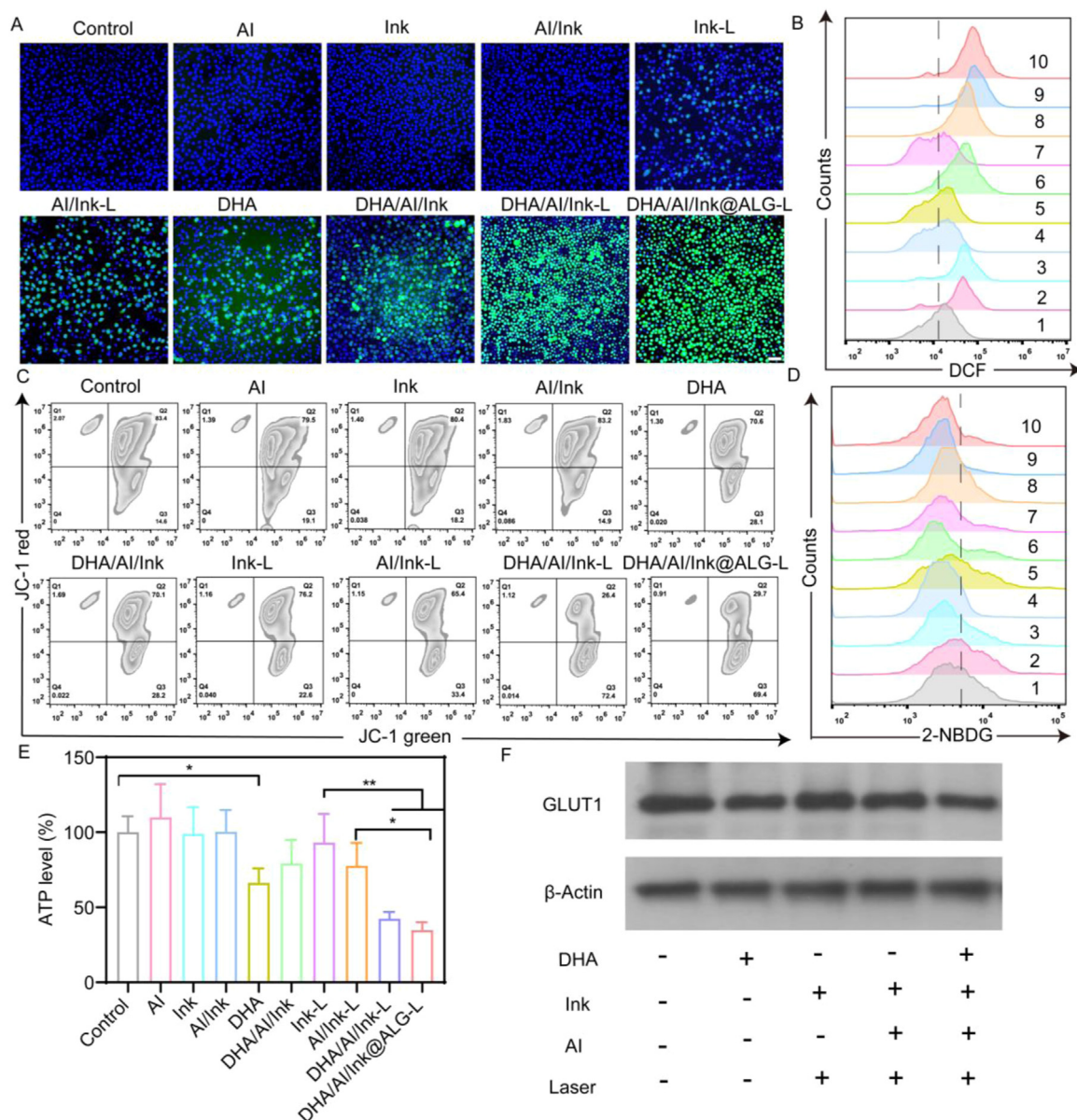


Fig. 4 – Exploration of DHA/AI/Ink@ALG-induced starvation therapy. (A) DCFH-DA was employed as a probe to detect ROS production in HepG2 cells treated with different agents (Scale bars = 50 μ m). (B) Flow cytometry analysis of ROS generation in HepG2 cells treated with different preparations (1: control; 2: Ink-L; 3: AI/Ink-L; 4: AI; 5: Ink; 6: DHA/AI/Ink; 7: AI/Ink; 8: DHA; 9: DHA/AI/Ink-L; 10: DHA/AI/Ink@ALG-L). (C) JC-1 was utilized to determine the changes in $\Delta\psi_m$ of HepG2 cells after treatment with different formulations. (D) Glucose uptake was monitored by 2-NBDG probe after HepG2 cells were treated with diverse formulations (1: control; 2: AI; 3: AI/Ink; 4: DHA; 5: Ink; 6: Ink-L; 7: AI/Ink-L; 8: DHA/AI/Ink; 9: DHA/AI/Ink-L; 10: DHA/AI/Ink@ALG-L). (E) Intracellular ATP levels of HepG2 after distinct treatments. (F) Intracellular GLUT1 expression was monitored by western blot. * $P < 0.05$, ** $P < 0.01$.

that alkyl radicals promoted DHA-induced suppression of glucose uptake. Furthermore, we conducted immunoblotting experiments to investigate whether the decrease in glucose uptake was attributed to the inhibition of GLUT1 expression by DHA. As illustrated in Fig 4F and S9, the reduction in GLUT1 expression by DHA treatment compared to control indicated the feasibility of DHA in closing the GLUT1 valve, which was consistent with previous studies [34]. Interestingly, GLUT1 expression was notably diminished after DHA/AI/Ink-L treatment, implying that R' further enhanced the suppression

of glucose uptake from the extracellular matrix induced by DHA.

3.5. Immobilization and photothermal properties of hydrogels in vivo and anti-tumor performance

The detrimental effects of intra-tumor drug injections on surrounding healthy tissue as they gradually disperse into the interstitium are well-documented. However, our study introduces a promising approach involving ALG, which can

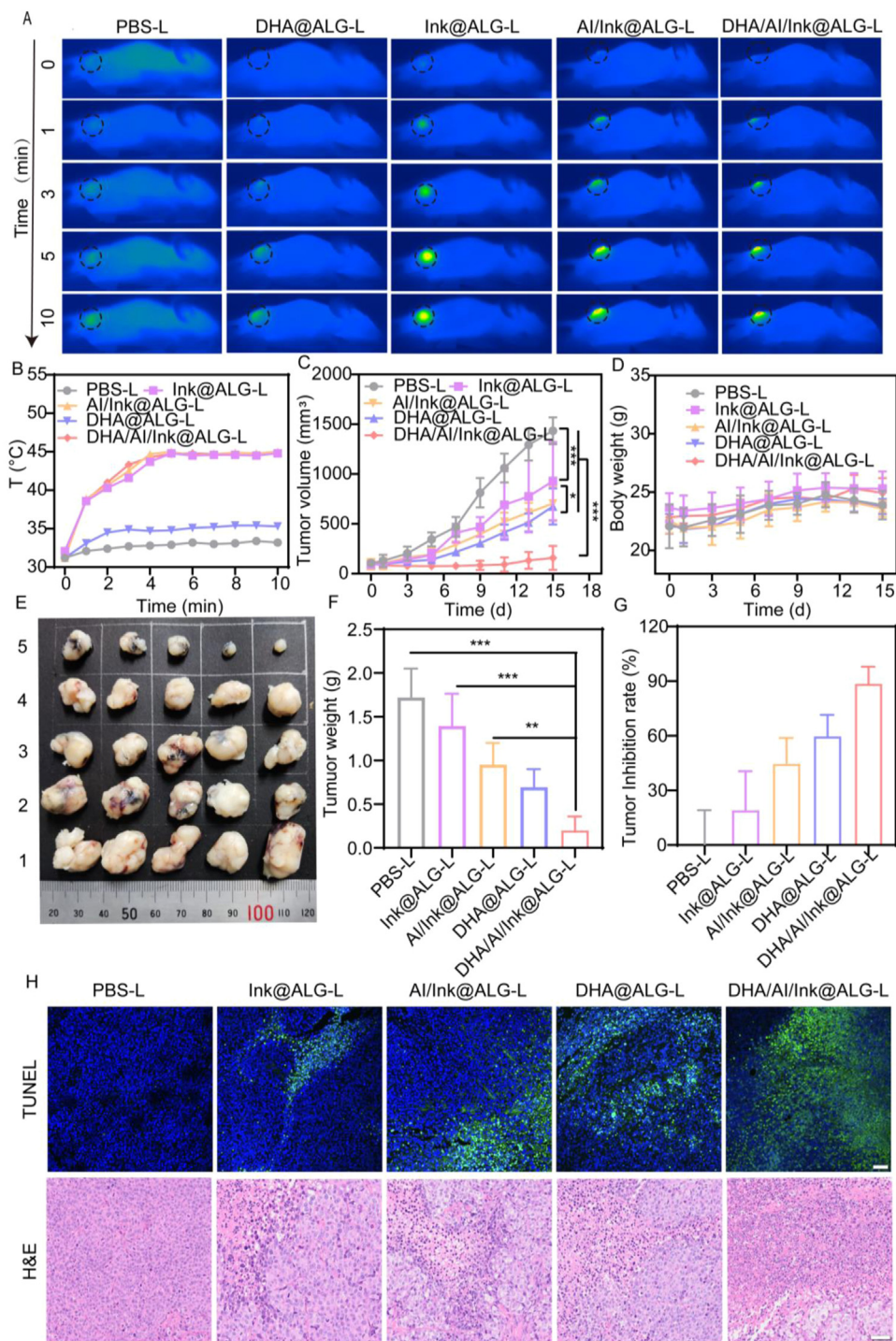


Fig. 5 – Photothermal efficiency and anti-tumor effect in vivo. (A) Photothermal pictures of DHA/AI/Ink@ALG gel in vivo at 1064 nm laser irradiation for 10 min and (B) the curve of temperature change. Variation in (C) tumor volume and (D) body weight of mice during 15-d treatment. After 15-d treatment the tumor tissue was removed and (E) photographed (1: PBS-L; 2:Ink@ALG-L; 3:AI/Ink@ALG-L; 4:DHA@ALG-L; 5:DHA/AI/Ink@ALG-L) and (F) weighed. (G) Tumor inhibition rates after treatment by distinct groups. (H) TUNEL and H&E staining of tumor tissues (scale bar: TUNEL = 20 μ m; H&E = 50 μ m). * $P < 0.05$, ** $P < 0.01$, *** $P < 0.001$.

readily bind to Ca^{2+} *in vivo* and form an in-situ hydrogel. This hydrogel effectively immobilizes the drug within the tumor, facilitating the accumulation of the drug. In order to assess the practicality of in-situ gelation and curing effects, we performed an experiment using a common fluorescent dye, indocyanine green (ICG), to simulate the diffusion process of a therapeutic agent in the tumor. Fig. S10 demonstrated that when ICG was administered alone, it diffused into the neighboring tissues within 4 h. On the other hand, the ICG@ALG group exhibited sustained fixation for 48 h, showcasing the remarkable ability of the ALG hydrogel to immobilize the drug within the tumor and enhance drug accumulation. Consequently, the utilization of ALG as a drug carrier presents a promising means of delivering drugs, ultimately increasing their potential effectiveness. To further investigate the drug-locking capability of ALG, subcutaneous injections of Ink and Ink@ALG were administered to mice, respectively. The skin tissue was dissected 48 h post-injection and the findings revealed that Ink had diffused extensively to the neighboring tissues. In contrast, the Ink@ALG group exhibited remarkable drug immobilization properties (Fig. S11).

To assess the *in vivo* photothermal characteristics of Ink, near infrared imaging equipment was utilized to monitor the temperature changes. As depicted in Fig. 5A, the temperature of the DHA@ALG group exhibited a slight increase in comparison to the PBS group, which probably due to the insulating effect of ALG. Promisingly, upon exposure to the photothermal agent Ink, the AI/Ink@ALG and DHA/AI/Ink@ALG groups displayed a notable temperature escalation and maintained a temperature of approximately 44 °C following 10 min of laser irradiation. These findings suggested that AI could be broken down into alkyl radicals *in vivo*.

Emboldened by the results of *in vitro* cytotoxicity assays, we proceeded to study the anti-tumor effects of DHA/AI/Ink@ALG *in vivo*. Once the tumors' size reached approximately 100 cm^3 , the mice were arbitrarily classified into 6 groups and administered different treatments: PBS-L, Ink@ALG-L, AI/Ink@ALG-L, DHA@ALG-L, DHA/AI/Ink@ALG-L. The treatment procedure was as follows: on days 0 and 3, different formulations were injected into the tumors and illuminated for 10 min. After 15 d, the neoplasms were excised, photographed, and weighed. As seen in Fig. 5C, the Ink@ALG-L group had a better tumor suppression efficacy compared to the PBS group, with a tumor inhibition ratio of approximately 19.05%. This outcome was ascribed to the low photothermal effect, which inhibited tumor growth but was not sufficient to eliminate the tumors entirely. Furthermore, the AI/Ink@ALG and DHA@ALG groups showed some mild anti-tumor effects, with tumor inhibition percentages of approximately 44.60% and 59.64%, respectively (Fig. 5G). The tumor size was visually represented by tumor weights and photos in Fig. 5E-F. Remarkably, the DHA/AI/Ink@ALG group markedly restricted the tumor proliferation, with a neoplasm suppression ratio of 88.50% (Fig. 5G). This experimental result indicated that R' boosted the DHA-induced cellular starvation to achieve a strong tumor suppression effect. Hematoxylin and Eosin (H&E) and terminal deoxynucleotidyl transferase dUTP nick end labeling (TUNEL) assays were

used to evaluate tumor histopathological damage. As shown in Fig. 5H-E, most of the cells in Ink@ALG-L, DHA@ALG-L, and AI/Ink@ALG-L maintained normal cell morphology compared to the PBS-L group. In contrast, the DHA/AI/Ink-L group exhibited large apoptotic cells with noticeable nuclear sequestration and sparse cellular arrangement. To further explore the ROS production following different treatments, DHE was utilized for fluorescence staining. As shown in Fig. S12, no significant green fluorescence was observed with PBS, but the DHA@ALG-L and AI/Ink@ALG-L groups produced mild fluorescence intensity, indicating that a fraction of ROS was produced upon treatment. Furthermore, the DHA/AI/Ink@ALG-L group displayed a substantial increase in green fluorescence compared to the DHA@ALG-L and AI/Ink@ALG-L groups, implying a synergistic production of ROS through the catabolism of R' by AI and DHA. This was in accordance with the *in vitro* experimental results. Based on the above experimental outcomes, it can be inferred that the catabolism of R' by DHA/AI/Ink@ALG under 1064 nm laser irradiation contributes to the induction of mitochondrial oxidative stress through the generation of ROS by DHA. There was no significant weight loss observed in the mice over the therapeutic period, suggesting that the hydrogels had no apparent systemic toxicity (Fig. 5D). In addition, histopathological studies of the major organs following 15d therapy revealed no visible tissue damage or inflammatory reactions in the treated mice (Fig. S13). Based on these findings, we conclude that DHA/AI/Ink@ALG demonstrated the most potent antitumor effect compared to all other experimental groups.

4. Conclusion

In conclusion, a stable and controllable functional hydrogel was developed that employs a tumor valve shut-down strategy to achieve starvation therapy for cancer. This hydrogel is composed of DHA, an inhibitor of GLUT1, an initiator of R' and Ink encapsulated within the ALG. Upon low-temperature photothermal heating, AI rapidly decomposed into R', which exacerbated the damage of DHA-induced mitochondrial oxidative stress by generating ROS. At the same time, R' enhanced DHA-induced starvation therapy by inhibiting GLUT1, which resulted in a decrease in glucose uptake. This "valve-off" strategy for amplifying tumor-specific starvation provides a promising paradigm for efficient and less toxic cancer therapy.

Conflicts of interest

The authors declare that they have no known competing financial interests or personal relationships that could have influenced the work reported herein.

Acknowledgements

Funding support was provided by the National Natural Science Foundation of China (grant no. 82071915), the Guang Dong Basic and Applied Basic Research Foundation (grant no.

2022A1515220015), and the Zhuhai City Department of science and technology (grant no. 2220004000131). The authors thank Shiyanjia Lab (www.shiyanjia.com) for the support of SEM test.

Supplementary materials

Supplementary material associated with this article can be found, in the online version, at doi:10.1016/j.ajps.2023.100850.

REFERENCES

- [1] Yu S, Chen Z, Zeng X, Chen X, Gu Z. Advances in nanomedicine for cancer starvation therapy. *Theranostics* 2019;9(26):8026–47.
- [2] Bononi G, Masoni S, Di Bussolo V, Tuccinardi T, Granchi C, Minutolo F. Historical perspective of tumor glycolysis: a century with Otto Warburg. *Semin Cancer Biol* 2022;86(Pt 2):325–33.
- [3] Fu LH, Qi C, Lin J, Huang P. Catalytic chemistry of glucose oxidase in cancer diagnosis and treatment. *Chem Soc Rev* 2018;47(17):6454–72.
- [4] Zhang C, Ni D, Liu Y, Yao H, Bu W, Shi J. Magnesium silicide nanoparticles as a deoxygenation agent for cancer starvation therapy. *Nat Nanotechnol* 2017;12(4):378–86.
- [5] Fu LH, Qi C, Hu YR, Lin J, Huang P. Glucose oxidase-instructed multimodal synergistic cancer therapy. *Adv Mater* 2019;31(21):1808325.
- [6] Wang M, Wang D, Chen Q, Li C, Li Z, Lin J. Recent advances in glucose-oxidase-based nanocomposites for tumor therapy. *Small* 2019;15(51):1903895.
- [7] Deng D, Xu C, Sun P, Wu J, Yan C, Hu M, et al. Crystal structure of the human glucose transporter GLUT1. *Nature* 2014;510(7503):121–5.
- [8] Reckzeh ES, Waldmann H. Development of glucose transporter (GLUT) inhibitors. *European J Org Chem* 2020;2020(16):2321–9.
- [9] Carvalho KC, Cunha IW, Rocha RM, Ayala ER, Cajaiba MM, Begnami MD, et al. GLUT1 expression in malignant tumors and its use as an immunodiagnostic marker. *Clinics* 2011;66(6):965–72.
- [10] Bridgford JL, Xie SC, Cobbold SA, Pasaje FMA, Herrmann S, Yang T, et al. Artemisinin kills malaria parasites by damaging proteins and inhibiting the proteasome. *Nat Commun* 2018;9(1):3801.
- [11] Dai X, Zhang X, Chen W, Chen Y, Zhang Q, Mo S, et al. Dihydroartemisinin: a potential natural anticancer drug. *Int J Biol Sci* 2021;17(2):603–22.
- [12] Yang Y, Zhu W, Dong Z, Chao Y, Xu L, Chen M, et al. 1D coordination polymer nanofibers for low-temperature photothermal therapy. *Adv Mater* 2017;29(40):1703588.
- [13] Wang Y, Chen F, Zhou H, Huang L, Ye J, Liu X, et al. Redox dyshomeostasis with dual stimuli-activatable dihydroartemisinin nanoparticles to potentiate ferroptotic therapy of pancreatic cancer. *Small Methods* 2022;7(5):2200888.
- [14] Bai S, Lu Z, Jiang Y, Shi X, Xu D, Shi Y, et al. Nanotransferrin-based programmable catalysis mediates three-pronged induction of oxidative stress to enhance cancer immunotherapy. *ACS Nano* 2022;16(1):997–1012.
- [15] Brown JM, Wilson WR. Exploiting tumour hypoxia in cancer treatment. *Nat Rev Cancer* 2004;4(6):437–47.
- [16] Shen S, Zhu C, Huo D, Yang M, Xue J, Xia Y. A hybrid nanomaterial for the controlled generation of free radicals and oxidative destruction of hypoxic cancer cells. *Angew Chem Int Ed Engl* 2017;56(30):8801–4.
- [17] Xiang H, Lin H, Yu L, Chen Y. Hypoxia-irrelevant photonic thermodynamic cancer nanomedicine. *ACS Nano* 2019;13(2):2223–35.
- [18] Ouyang B, Liu F, Ruan S, Liu Y, Guo H, Cai Z, et al. Localized free radicals burst triggered by NIR-II light for augmented low-temperature photothermal therapy. *ACS Appl Mater Interfaces* 2019;11(42):38555–67.
- [19] Pan H, Zhang C, Wang T, Chen J, Sun SK. In situ fabrication of intelligent photothermal indocyanine green-alginate hydrogel for localized tumor ablation. *ACS Appl Mater Interfaces* 2019;11(3):2782–9.
- [20] Abasalizadeh F, Moghaddam SV, Alizadeh E, Akbari E, Kashani E, Fazljou SMB, et al. Alginate-based hydrogels as drug delivery vehicles in cancer treatment and their applications in wound dressing and 3D bioprinting. *J Biol Eng* 2020;14:8.
- [21] Shao J, Ruan C, Xie H, Li Z, Wang H, Chu PK, et al. Black-phosphorus-incorporated hydrogel as a sprayable and biodegradable photothermal platform for postsurgical treatment of cancer. *Adv Sci* 2018;5(5):170084.
- [22] Qian Q, Wang D, Shi L, Zhang Z, Qian J, Shen J, et al. A pure molecular drug hydrogel for post-surgical cancer treatment. *Biomaterials* 2021;265:120403.
- [23] Zhang C, Shi G, Zhang J, Song H, Niu J, Shi S, et al. Targeted antigen delivery to dendritic cell via functionalized alginate nanoparticles for cancer immunotherapy. *J Control Release* 2017;256:170–81.
- [24] Wang S, Cao Y, Zhang Q, Peng H, Liang L, Li Q, et al. New application of old material: Chinese traditional ink for photothermal therapy of metastatic lymph nodes. *ACS Omega* 2017;2(8):5170–8.
- [25] Pawar SN, Edgar KJ. Alginate derivatization: a review of chemistry, properties and applications. *Biomaterials* 2012;33(11):3279–305.
- [26] Chao Y, Xu L, Liang C, Feng L, Xu J, Dong Z, et al. Combined local immunostimulatory radioisotope therapy and systemic immune checkpoint blockade imparts potent antitumour responses. *Nat Biomed Eng* 2018;2(8):611–21.
- [27] Funami T, Fang Y, Noda S, Ishihara S, Nakauma M, Draget KI. Rheological properties of sodium alginate in an aqueous system during gelation in relation to supermolecular structures and Ca²⁺ binding. *Food Hydrocoll* 2009;23(7):1746–55.
- [28] Lee KY, Mooney DJ. Alginate: properties and biomedical applications. *Prog Polym Sci* 2012;37(1):106–26.
- [29] Boi S, Rouatbi N, Dellacasa E, Di Lisa D, Bianchini P, Monticelli O, et al. Alginate microbeads with internal microvoids for the sustained release of drugs. *Int J Biol Macromol* 2020;156:454–61.
- [30] Cao Y, Song W, Jiang Q, Xu Y, Cai S, Wang S, et al. Nanoparticles from ancient ink endowing a green and effective strategy for cancer photothermal therapy in the second near-infrared window. *ACS Omega* 2020;5(11):6177–86.
- [31] Li Y, Li M, Liu L, Xue C, Fei Y, Wang X, et al. Cell-specific metabolic reprogramming of tumors for bioactivatable ferroptosis therapy. *ACS Nano* 2022;16(3):3965–84.
- [32] Suski J, Lebedzinska M, Bonora M, Pinton P, Duszynski J, Wieckowski MR. Relation between mitochondrial membrane potential and ROS formation. *Methods Mol Biol* 2018;1782:357–81.
- [33] Liu Y, Sun Y, Guo Y, Shi X, Chen X, Feng W, et al. An Overview: the diversified role of mitochondria in cancer metabolism. *Int J Biol Sci* 2023;19(3):897–915.
- [34] Li Y, Pei Q, Cui B, Zhang H, Han L, Li W, et al. A redox-responsive dihydroartemisinin dimeric nanopropdrug for enhanced antitumor activity. *J Nanobiotechnology* 2021;19(1):441.